Charge Carrier Dynamics of Photoexcited Co_3O_4 in Methanol: Extending High Harmonic Transient Absorption Spectroscopy to Liquid Environments

L. Robert Baker†, Chang-Ming Jiang†, Stephen T. Kelly ∥ , J. Matthew Lucas‡, Josh Vura-Weis†, Mary K. Gilles ∥ , A. Paul Alivisatos† ⊥ , and Stephen R. Leone* †§ ∥

†Department of Chemistry, ‡Department of Mechanical Engineering, and §Department of Physics, University of California, Berkeley, Berkeley, California 94720, United States

∥Chemical Sciences and ⊥Materials Sciences Division, Lawrence Berkeley National Lab, Berkeley, California 94720, United States

DOI: 10.1021/nl502817a

*E-mail srl@berkeley.edu. Phone (510) 643-5467. Fax (510) 643-1376.

•

Abstract

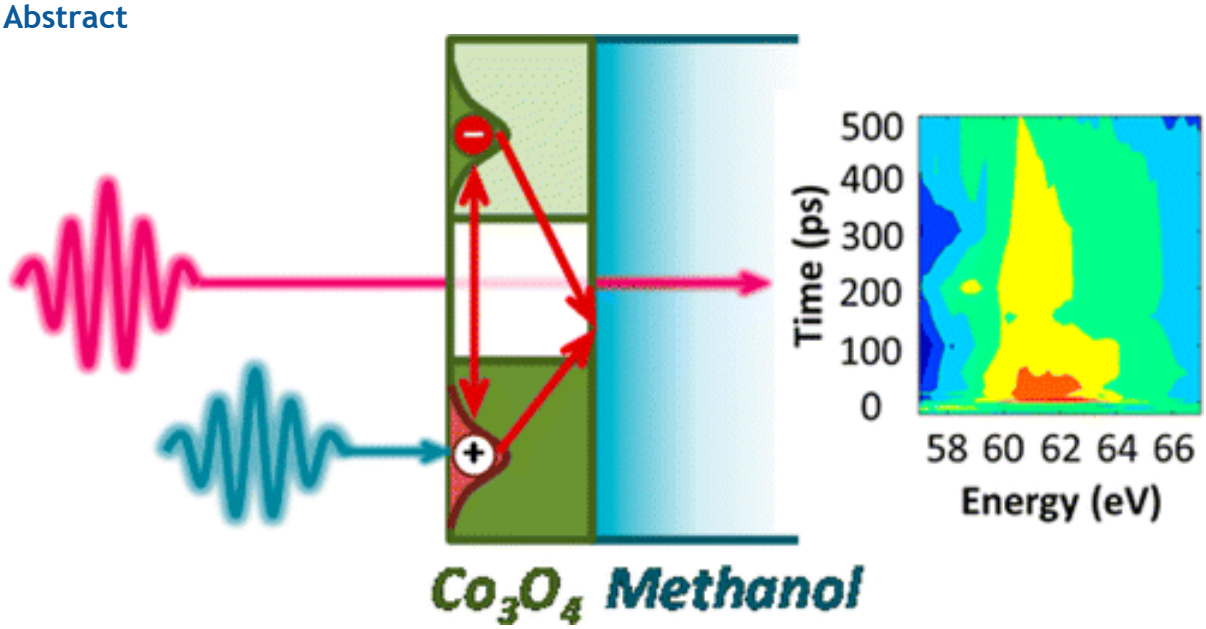

Charge carrier dynamics in Co_3O_4 thin films are observed using high harmonic generation transient absorption spectroscopy at the Co $M_{2,3}$ edge. Results reveal that photoexcited Co_3O_4 decays to the ground state in 600 ± 40 ps in liquid methanol compared to 1.9 ± 0.3 ns in vacuum. Kinetic analysis suggests that surface-mediated relaxation of photoexcited Co_3O_4 may be the result of hole transfer from Co_3O_4 followed by carrier recombination at the Co_3O_4–methanol interface.

Keywords: High harmonic generation; **transient absorption spectroscopy**;

surface states; **interfacial charge transfer**; **photocatalysis**; **ligand-to-metal charge transfer**

Understanding charge carrier dynamics at interfaces is scientifically and technologically important because these dynamics govern the efficiency of materials for nearly all energy conversion and charge-based device applications.(1, 2) Fuel cells,(3, 4) batteries,(5, 6) electrocatalysts,(7, 8) photocatalysts,(9) and photovoltaic devices(10) are each examples of systems that rely on interfacial charge transfer to drive an energy conversion process. Efficiency losses that currently plague devices for many energy applications are a result of poorly understood carrier dynamics at the active catalytic or device interface.(11-18) In addition to energy conversion processes, carrier dynamics in interface states also control the optoelectronic properties of many materials.(19, 20) For example, the optical properties of a nanoparticle are dramatically affected by relaxation pathways in surface states such that fluorescence yields can be tuned from zero to almost unity efficiency simply by controlling the coverage and type of the molecular passivation layer on the nanoparticle surface.(21, 22) This has long suggested that decay pathways through surface states can dominate bulk carrier lifetimes in nanoscale systems.

Because surface electronic structure strongly influences the catalytic and optical properties of materials, it is important to develop in situ probes capable of measuring electron dynamics of materials under relevant environmental conditions. This is because the surface electronic structure depends strongly on adsorption and interface bonding, and the same material may exhibit very different properties depending on the chemical nature of the interface, which changes in various gas or liquid conditions.(23-25) Ultrafast optical spectroscopy has been used to observe charge carrier kinetics in catalysts under working conditions.(26-29) Ultrafast methods in the visible and IR spectral regions are well established for observing charge carrier kinetics in condensed phases. For example, transient mid-IR absorption spectroscopy is commonly used to probe the kinetics of excited conduction band electrons in high bandgap semiconductors.(30, 31) Visible and near IR spectroscopy has also been used to measure the kinetics of free and trapped holes in semiconductor materials,(28, 32) and bound exciton dynamics have been observed using broadband white light transient absorption spectroscopy.(33, 34) While each of these methods can measure the kinetics of transient features on the ultrafast time scale, they often cannot be used to determine the chemical nature of the excited state dynamics. This is because charge carriers give rise to broad features in the visible and IR spectral range that cannot be used to determine oxidation state, spin state, or charge localization to specific elements.

Alternatively, X-ray based techniques have the significant advantage of being element specific as well as extremely sensitive to the oxidation and spin state of a system.(27, 28) Recently, table-top high harmonic generation (HHG) spectroscopy in the extreme ultraviolet (EUV) spectral range has convincingly demonstrated the ability to combine the ultrafast time resolution of optical methods with the electronic structure sensitivity of X-ray techniques to probe

detailed carrier dynamics in solid-state semiconductor systems.(35) We now further extend the ability of HHG spectroscopy to include in situ measurements in the liquid phase. This new capability extends the use of HHG spectroscopy to study a wide range of catalytic and energy conversion processes that occur at the solid–liquid interface.

In the present report, we describe the use of a liquid flow cell in a table-top HHG transient absorption spectrometer to probe charge carrier relaxation dynamics of Co_3O_4 thin films (15 nm thick) in liquid methanol. Comparing transient absorption spectra of identical Co_3O_4 thin films in vacuum and methanol environments reveals that, in the presence of liquid methanol, a photoexcited Co_3O_4 thin film returns to the ground state with a time constant of 600 ± 40 ps, which is more than 3 times faster than the value of 1.9 ± 0.3 ns observed in vacuum. In this study, methanol was selected as a solvent instead of water because methanol is known to be an efficient hole acceptor from photoexcited metal oxides.(36-38) Because the current experimental setup did not allow for exchange of solvents in the liquid cell owing to the very low flow rates, it was not possible to measure the effect of various solvents on the Co_3O_4 kinetics in this experiment. However, a solvent-dependent experiment would clearly add additional insights, and we hope that this experiment may be realized in the future.

In a perfectly continuous 15 nm Co_3O_4 thin film, the surface layer would represent <2% of the entire sample. TEM images show that in the present studies the film contains pinholes (see Supporting Information Figure S10), and from these images we estimate that the actual surface-to-bulk ratio may be as high as 10%. This surface layer may affect the observed carrier dynamics in a variety of ways. First, interface adsorption of methanol may alter the surface electronic structure of Co_3O_4, giving rise to possible surface-mediated carrier relaxation pathways that are measurably faster than the bulk exciton decay rate.(19, 20) Alternatively, it is possible that by polarizing the interface(39, 40) the surface methanol layer induces a change in the dielectric function across some screening depth of the Co_3O_4 thin film, which can change the interaction and relaxation time scale of excitons even in the bulk Co_3O_4 film. Below we analyze kinetics of carrier relaxation in vacuum and methanol and discuss the possible mechanisms for enhanced carrier relaxation in methanol. Although the current experiment is unable to completely distinguish between surface and bulk carrier relaxation dynamics, we show that surface-mediated relaxation of the exciton via hole transfer from the Co_3O_4 to the methanol is a possible mechanism for the observed decay kinetics.

During an electrochemical reaction, kinetic barriers to charge injection result in required overpotentials that adversely affect the efficiency of electrochemical energy conversion.(41, 42) An important example is the oxidative overpotential necessary for water electrolysis on noble metal catalysts that severely limits the

efficiency of the O_2 evolution reaction. Recent discoveries have shown that the required overpotential for O_2 evolution is significantly decreased if certain 3d transition metal catalysts are used in place of Pt or other noble metal anodes.(7, 43) Since this discovery, Co_3O_4 in particular has drawn much attention as a highly efficient, earth abundant oxidation catalyst.(44-47)

Co_3O_4 is also photocatalytically active for the O_2 evolution reaction. However, in this case dye-sensitized Co_3O_4 nanoparticles are used rather than the pure metal oxide. In these organic dye–Co_3O_4 tandem photocatalysts, the dye (often $[Ru(bpy)_3]^{2+}$) acts as the primary light absorber, and following photoexcitation a hole is transferred from the dye to the Co_3O_4 catalyst.(48) In this way, the hole can reside in the valence band of Co_3O_4 sufficiently long to inject to the reactant, and electron–hole pair recombination does not occur because the electron remains localized on the excited dye molecule. In these systems, the turnover number is severely limited by the stability of $[Ru(bpy)_3]^{2+}$, which photodegrades much faster than the highly stable Co_3O_4 nanoparticles.(48, 49) However, although Co_3O_4 has a band gap of only 1.6 eV, direct illumination of Co_3O_4 without $[Ru(bpy)_3]^{2+}$ or of $[Ru(bpy)_3]^{2+}$ without Co_3O_4 yields no reaction products.(46, 48, 50)

According to the above observations, it has been assumed, although never measured, that bulk exciton recombination in photoexcited Co_3O_4 is much faster than hole injection to the reactant. However, in the present study we show that there may exist a surface-mediated relaxation pathway that is measurably faster than the bulk exciton recombination in vacuum, suggesting that photoexcited charge carriers interact with surface states within their recombination lifetime. We also consider several possible mechanisms for this surface-mediated recombination pathway.

In related work, the short time photophysics of Co_3O_4 in vacuum is considered, as discussed further below.(51) Here the long-time dynamics in methanol versus vacuum is measured. Figure 1 shows contour plots of the transient absorption dynamics at the Co $M_{2,3}$ edge following photoexcitation of a Co_3O_4 thin film with a 400 nm laser pulse. Part A presents results for the Co_3O_4 film in the methanol flow cell while part B shows results for an identical film in vacuum. Parts C and D show the results of a global fit (described below) to the corresponding data sets. Two differences between the methanol and the vacuum samples are apparent from these contour plots: First, a bleach is observed at the low energy side of the spectrum in methanol below approximately 58 eV. A control experiment in which transient absorption in methanol is measured in a liquid flow cell containing no Co_3O_4 thin film shows that this response is due to the methanol rather than the

Co_3O_4. This may be a result of two-photon absorption by the methanol at 400 nm due to the high excitation powers used in this experiment, and the results of this experiment are shown in Supporting Information Figure S1. The second difference is that the transient absorption feature centered at 62 eV in both samples at a delay time of 1 ps shifts to lower energy by 1.5 eV and subsequently decays faster in methanol than in vacuum. This feature, which is absent in methanol without Co_3O_4, reflects the photoinduced carrier dynamics in the Co_3O_4 thin film. Figure 2 further illustrates the different spectral kinetics observed for Co_3O_4 in methanol and in vacuum by showing transient spectra of both samples taken at select time points (parts A–D) and kinetic traces at two different absorption energies (parts E–F).

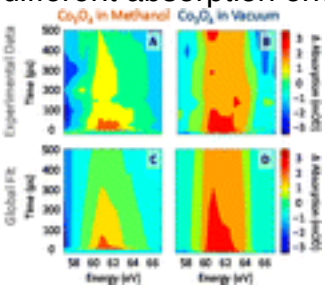

Figure 1. Contour plots showing the transient absorption of Co_3O_4 in methanol and in vacuum at the Co $M_{2,3}$ edge following photoexcitation with a 400 nm pump pulse at pump–probe delay times up to 500 ps. Parts A and B show the experimental data, and parts C and D show the results for a global fit of the corresponding data sets using a 2-component, sequential model. The color scale represents ΔA in units of mOD. The global fit does not incorporate all the features of the kinetic models in Scheme 1.

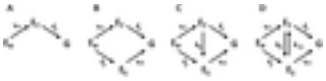

Scheme 1

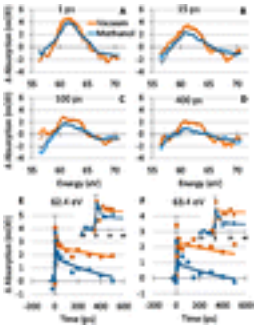

Figure 2. (A–D) Transient absorption spectra of Co_3O_4 in methanol and vacuum at pump–probe delay times of 1 (A), 15 (B), 150 (C), and 400 (D) ps. The broad, light-colored lines represent the experimental spectra, while the narrow, dark-

colored lines represent the global fit values at the corresponding time slices. (E,F) Kinetic traces of Δ*A* at 62.4 eV (E) and 63.4 eV (F) highlighting the different spectral evolution of the Co_3O_4 sample in vacuum and methanol. Insets on E and F are an enlargement of the data at time delays out to 40 ps.

To quantify these kinetic and spectral differences, a global fit is performed using a two-component sequential model with the GLOTARAN software package.(52) We find that a model containing at least two kinetic steps is necessary to fit the transient absorption traces. To summarize the two-component sequential model, it assumes that a direct rise occurs to an initial state within an instrument response time ≪1 ps; this rise is then followed by a decay from the initial state to an intermediate state at a first time constant, τ_1, which is subsequently followed by decay from the intermediate state back to the ground at a second time constant, τ_2. In this method, the spectral shapes of the initial and intermediate states as well as the corresponding rate constants are determined by a least-squares fit to the two-dimensional data set. Note that this kinetic model is identical to the process shown in Scheme 1A.

The results of the global fit for Co_3O_4 in methanol and in vacuum are shown Figure 3. Parts A and B show the two spectral components corresponding to the initial and intermediates states for the methanol and vacuum cases, respectively, and the insets represent the kinetic traces showing the time dependent evolution of these states. To summarize the kinetics, it is found that in vacuum the initial state decays to an intermediate state with a time constant of 8 ± 2 ps and that the intermediate state subsequently decays to the ground state with a time constant of 1.9 ± 0.3 ns. By comparison, in methanol the initial state decays to a spectrally different intermediate state in 4.9 ± 0.9 ps and that intermediate state subsequently decays to the ground state in 600 ± 40 ps. Error values represent standard errors calculated by the root-mean-square method using the GLOTARAN statistical software package.

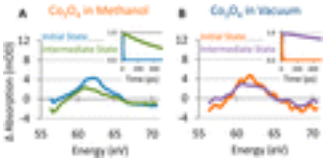

Figure 3. Transient absorption spectra of the initial and intermediate states determined by the two-component, sequential fit of the experimental data taken for Co_3O_4 in methanol (A) and vacuum (B). The insets show the corresponding time-dependent evolution of these states. In the case of Co_3O_4 in methanol, the initial and intermediate states decay with time constants of 4.9 ± 0.9 and 600 ± 40 ps, respectively. By contrast, in the case of Co_3O_4 in vacuum, the initial and intermediate states decay with time constants of 8 ± 2 ps and 1.9 ± 0.3 ns, respectively. Error values represent the standard errors calculated from the global fit using the GLOTARAN statistical software package.

Comparing the spectra shown in parts A and B of Figure 3, it can be seen that

the initial state spectra are very similar for Co_3O_4 samples in both methanol and vacuum (see also Figure 2A). This indicates that the interface does not determine the initial photoexcited state of the system and the effect of the interface on the carrier dynamics is not significant during the first 1 ps following photoexcitation. As noted, the transient dynamics of Co_3O_4 in vacuum were investigated in detail on the sub-ps time scale using the same experimental apparatus with a time resolution down to 45 fs.(51) To summarize those results here two different processes are observed in the HHG transient absorption spectrum on the sub-ps time scale: (1) The intensity of the transient absorption signal decreases by ~60%, and this amplitude decay occurs in 190 ± 10 fs. This amplitude decay is also found to occur more rapidly at higher excitation fluence, which is consistent with electron–hole pair recombination via an Auger decay mechanism. It is hypothesized that the 190 fs time constant associated with Auger decay corresponds to exciton localization, which limits subsequent multiexciton interactions in the Co_3O_4 sample. (2) In addition to the amplitude decay, a 200 meV red shift of the transient absorption occurs in 535 ± 33 fs, and this process is ascribed to hot carrier thermalization by carrier–phonon scattering. Here we consider the longer-time effects on the exciton recombination dynamics with a comparison of the methanol and vacuum interfaces.

Examination of the intermediate states on longer time scales shows that for the Co_3O_4 sample in vacuum, little spectral evolution occurs during the entire time evolution, as indicated by the close similarity between the initial and intermediate spectra of this sample (see Figure 3B). The only difference between these two spectra is a slight decay of the peak center at 62 eV. The experiments on the sub-ps time scale show that this effect is most pronounced within the first few hundred femtoseconds after excitation, and here we observe that a tail of this decay extends out to approximately 10 ps. This fast decay to the intermediate state in vacuum is attributed to Auger recombination accompanied by hot carrier thermalization, as discussed in detail separately.(51) The close similarity between the initial and intermediate spectra for the results in vacuum indicate that the two components of the global fit represent similar electronic states with the small differences resulting primarily from Auger decay and carrier thermalization.

Different results are observed for Co_3O_4 samples in methanol. This is seen in Figure 3A, which shows that the peak in transient absorption originally centered at 62 eV decays asymmetrically from the high-energy side, causing it to shift to ~1.5 eV lower energy in the intermediate spectrum of this sample. Because these transient kinetics give rise to an intermediate spectrum that is only observed for Co_3O_4 in methanol, we conclude that the presence of liquid methanol on the Co_3O_4 surface gives rise to an additional electron–hole pair recombination pathway. To quantify the rate of elementary steps in this additional relaxation pathway, we consider several possible kinetic models.

It is likely that the time constants observed in methanol represent the combined rate of carrier relaxation in vacuum with additional decay processes that occur only in methanol. If this is true, the 4.9 and 600 ps time constants observed in the global fit represent combined rates of competing decay processes, and a more in-depth kinetic analysis is required to determine the actual rates of elementary steps. Models considered are shown in Scheme 1, which are discussed in detail below. Part A shows the simplest case observed in vacuum where an initial excited state, E_H, decays to an intermediate excited state, E_T, at a rate given by k_1, and E_T subsequently decays to the ground state, G, at a rate given by k_2. Values for k_1 and k_2 based on the global fit to the data obtained for Co_3O_4 in vacuum are given in Table 1 in units of ps^{-1}.

Table 1. Rate Constants for Kinetic Models Depicted in Scheme 1[a]

	k_1	k_2	k_3	k_4	k_5	k_{-5}
model A	1.2×10^{-1}	5.1×10^{-4}				
model B	1.2×10^{-1}	5.1×10^{-4}	7.9×10^{-2}			
model C	1.2×10^{-1}	5.1×10^{-4}	2.1×10^{-1}	1.7×10^{-3}	2.1×10^{-1}	0
model D	1.2×10^{-1}	5.1×10^{-4}	2.1×10^{-1}	$\geq 1.7 \times 10^{-3}$	2.1×10^{-1}	≥ 0

aAll values are given in units of ps^{-1}. No value is provided for k_4 in Model B because this model does not match the long-time behavior of the experimental data. The experimental data cannot differentiate between Models C and D, which differ only in the values of k_4 and k_{-5}.

Scheme 1B shows the case where a competing relaxation pathway is included. According to this model the initial excited state, E_H, can additionally decay to an intermediate state, E_S, at a rate given by k_3, and E_S subsequently decays to the ground state, G, at a rate given by k_4. Assuming this model, the intermediate state observed in the fit to the data obtained for Co_3O_4 in methanol would form at a rate given by $k_1 + k_3$ and represent a convolution of E_T and E_S with relative contributions given by $k_1/(k_1 + k_3)$ and $k_3/(k_1 + k_3)$, respectively. Because the formation of an intermediate state for Co_3O_4 in methanol occurs in 4.9 ± 0.9 ps and the value of k_1 is independently known, it would be possible to calculate k_3 and to deconvolute the intermediate spectrum observed for Co_3O_4 in methanol in terms of E_T and E_S. According to this model, the intermediate spectrum for Co_3O_4 in methanol, presumably a composite of both E_T and E_S, would show a biexponential decay to the ground state at rates given by k_2 and k_4. However, this predicted long-time behavior is not compatible with the results of Figure 2, which show that the composite intermediate spectrum can be fit with a single

exponential rate of 1.7×10^{-3} ps^{-1}. This rate is approximately 3 times faster than k_2 for Co_3O_4 samples measured in vacuum (5.1×10^{-3} ps^{-1}). Although model B cannot be entirely excluded, models C and D provide better fits to the experimental data at time delays >100 ps.

For the case of $k_3 = k_5$ in Scheme 1C this process can be solved in closed form, and the solution is provided in the Supporting Information. The results show that E_S will form at a rate given by k_3 and subsequently decays to the ground state at a rate given by k_4. This model provides a match to the observed transient kinetics for Co_3O_4 in methanol (see Supporting Information Figure S2). Other cases where $k_3 \neq k_5$ are also considered by numerical integration in the Supporting Information. The results show that k_3 and k_5 may differ at most by approximately 1 order of magnitude and still fit the data.

Lastly, we consider the case for a reversible step $E_T \rightleftarrows E_S$ at k_5/k_{-5} as shown in Scheme 1D. Using numerical integration, we find that it is possible to fit the experimental data using this model (see Supporting Information Figure S4). The results show that the values of k_1, k_2, k_3, and k_5 do not vary considerably between Scheme 1 panels C and D. However, the value of k_4 necessary to match the observed 600 ± 40 ps decay to the ground state increases linearly with the ratio k_{-5}/k_5 (see Supporting Information Figure S5). This suggests that the value of k_4 in Table 1 (1.7×10^{-3} ps^{-1}) for the case $k_{-5} = 0$ (i.e., Scheme 1C) represents a lower limit, and this rate constant is possibly faster if exciton interactions leading to an enhanced recombination rate are reversible. Because the data cannot differentiate between Scheme 1 panels C and D, it is only possible to give $k_4 = 1.7 \times 10^{-3}$ ps^{-1} as the lowest possible value for the rate of methanol-enhanced exciton recombination as shown in Table 1.

To better understand the chemical nature of charge carrier dynamics in these two systems it is valuable to interpret these transient spectra in terms of specific electronic excited states. Toward this end we employ the CTM4XAS55 ligand field multiplet model.(53) This model has also been used to interpret the sub-ps carrier dynamics in photoexcited Co_3O_4(51) and Fe_2O_3,(35) and we consider the results of these calculations further for Co_3O_4. To summarize the method, the CTM4XAS55 ligand field multiplet model is capable of predicting X-ray absorption spectra from the calculated splitting of metal d orbitals by the ligand field in an atomic cluster.(54, 55) Solid-state effects are included in this model simply as a reduction in the Slater integral term to account for electron correlation and charge transfer effects. However, because the current model relies on an atomic cluster picture, it is not expected to accurately predict X-ray spectra for surface states or trapped charges, which we observe on the several picoseconds time scale.

Co_3O_4 exists in the spinel structure where oxygen anions form a face-centered cubic lattice and cobalt cations occur in both the 2+ and 3+ valence states in a 1:2 ratio. Within the lattice, the Co^{2+} cations coordinate to four oxygen ions in a tetrahedral geometry, and the Co^{3+} cations coordinate to six oxygen ions in an octahedral geometry. Using the CTM4XAS55 program to match the ground state absorption spectrum of Co_3O_4 produces the fit shown in Figure 4A. In this fitting, the 10Dq ligand field values for Co ions at both tetrahedral and octahedral sites are taken from literature,(56) and the contribution to absorption from each valence state is normalized based on the d-level occupancy and the known stoichiometry. The absolute energy axis is scaled independently for each state to match the experimental spectrum. The Slater integral reduction and the Fano factor for line width broadening are also taken as adjustable parameters. Exact fitting parameters are provided in the Supporting Information.

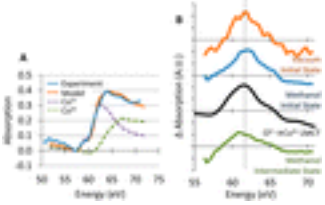

Figure 4. (A) Experimental ground state $M_{2,3}$ edge absorption spectrum of Co_3O_4 and corresponding fit using the ligand field multiplet model. The nonresonant absorption contributions extending from the valence electron ionization at ~20 eV have been subtracted from the raw spectrum. The dashed lines show the respective contributions of Co^{2+} (T_d) and Co^{3+} (O_h) cations to the simulated absorption spectrum. (B) Simulated difference spectrum for a Co^{3+} (O_h) LMCT excited state compared to the experimental transient absorption spectra for Co_3O_4 in methanol and vacuum. The simulated spectrum is an excellent match for both of the initial states. However, the intermediate state for the methanol sample is shifted to lower energy relative to the other three spectra and shows a bleach below ~58 eV.

All parameters are optimized based on the fit to the experimental ground state spectrum and then kept constant to predict the X-ray absorption spectra of various possible excited states. Excited state spectra are predicted by manually changing the valence state of cobalt ions in the different lattice sites to simulate the following excitations: (1) $O^{2-} \rightarrow Co^{3+}$ ligand-to-metal charge transfer (LMCT), (2) $O^{2-} \rightarrow Co^{2+}$ LMCT, (3) $Co^{3+} \rightarrow Co^{2+}$ metal-to-metal charge transfer (MMCT), and (4) $Co^{2+} \rightarrow Co^{3+}$ MMCT. In this notation, the arrow indicates an electron transfer between adjacent ions in the Co_3O_4 lattice. In addition, X-ray spectra of d–d excited states at both octahedral (5) and tetrahedral (6) lattice sites are also modeled by manually rearranging the d-shell electron configuration at fixed

occupancy by using Tanabe–Sugano diagrams also calculated in CTM4XAS55. The predicted spectra for each of these six possible photoexcited states are shown in Supporting Information Figure S7. Comparison of each of these modeled excited state spectra with the experimental X-ray transient absorption measurements reveals that the initial state in both the vacuum sample and the methanol sample represent an $O^{2-} \rightarrow Co^{3+}$ LMCT excitation (see Figure 4B), and this conclusion is consistent with previous assignments of the optical absorption bands in spinel Co_3O_4.(57)

This assignment indicates that, in the initial excited state of both samples, the hole resides in the O 2p orbital of the Co_3O_4 valence band and the electron resides in the Co 3d orbital of the conduction band. The current model is unable to predict spectra associated with surface states, charged layers, or multiexciton formation, and indeed we find that none of the six excited state spectra considered by the present model are a good match for the intermediate spectrum of the Co_3O_4 in liquid methanol. We now consider several possible mechanisms for the methanol-enhanced recombination pathway discussed above.

We consider three possible ways that the methanol surface layer can influence the electronic structure of Co_3O_4 as observed by the X-ray spectroscopy. First, an interface potential between the Co_3O_4 and the methanol layer could induce band bending in the Co_3O_4 thin film. This band bending would represent a driving force for charge separation, and electrons and holes would be pushed in opposite directions inside the Co_3O_4 film following photoexcitation. In the absence of a net catalytic reaction, this effect would be expected to lead to a longer, rather than shorter, carrier lifetime because charge separation would prevent electron–hole pair recombination. This is different than what we observe experimentally, so it is unlikely that charge separation due to band bending can be responsible for methanol-enhanced carrier recombination as observed in this experiment.

Second, it is possible that the methanol surface layer influences the dielectric function felt by excitons in the Co_3O_4 thin film. This could occur due to polarization of the Co_3O_4 surface by methanol adsorption, which would affect the dielectric function of the Co_3O_4 over some screening depth from the interface. In the case of a reduced dielectric constant in the Co_3O_4 film, neighboring excitons may interact(58) giving rise to an enhanced decay rate by biexciton or Auger recombination. However, based on the 190 fs time scale for Auger recombination and carrier localization observed in the related study,(51) we believe it is unlikely that multiexciton formation plays a significant role on the carrier dynamics at these much longer scales (tens to hundreds of ps). While current data cannot completely exclude this mechanism, it is probable that the surface states of the Co_3O_4–methanol interface are also affecting the observed carrier relaxation kinetics as discussed below.

Finally, we consider the formation of surface states in the Co_3O_4 thin film due to methanol adsorption that could act either as an electron or hole trap at the Co_3O_4–methanol interface. In this case, surface charge trapping followed by enhanced electron–hole pair recombination at the Co_3O_4–methanol interface could explain the spectral and dynamic experimental results. Assuming this mechanism, the rate constants k_3 and k_5 discussed above would represent the rate of surface charge trapping, and k_4 would represent the rate of subsequent electron–hole pair recombination at the Co_3O_4–methanol interface. To determine the plausibility of this explanation, it is possible to estimate the diffusion coefficient of charge carriers in Co_3O_4 based on the known film thickness and the measured rate of surface trapping. For a 15 nm thick film and a surface trapping rate between 7.9×10^{-2} and 2.1×10^{-1} ps^{-1} (see k_3 values in Table 1), the calculated charge carrier diffusion coefficient is between 0.059 and 0.15 $cm^2 s^{-1}$. This range of values encompasses the measured diffusion coefficient for photoexcited electrons in titanium oxide thin films.(59, 60) While carrier diffusion in Co_3O_4 is not expected to be identical to TiO_2, this correlation suggests that the observed time scale is roughly consistent with exciton migration to the surface by random walk diffusion.

To further explore this mechanism for surface-mediated carrier recombination, we consider what is known about the electronic structure of methanol adsorbed on metal oxides. We first consider the presence of unoccupied states near the Co_3O_4 conduction band edge that could act as electron traps. When methanol adsorbs on certain metals or metal oxides, discrete surface states appear above the Fermi level, and these states (sometimes called “wet electron” states) have been extensively studied by two-photon photoemission spectroscopy.(61, 62) However, it is improbable that these states act as an electron trap in the present experiment for two reasons: First, electron trap states at the metal oxide–methanol interface have only previously been reported several electronvolts above the conduction band minimum.(61) Because in the present experiment surface–charge interaction is occurring on a time scale slower than hot carrier thermalization, it is not likely that the photoexcited electrons would be able to access theses states that are much greater than kT above the conduction band minimum. Second, time-resolved studies of electrons trapped in these states show that they have very short lifetimes on the order of <100 fs.(61) However, in the present study, we observe a much longer time scale (~5 ps) for surface charge interactions. Consequently, it is unlikely that electron trapping in methanol leads to surface-mediated carrier recombination as observed in this experiment.

We last consider the possibility of hole trapping at the Co_3O_4 surface. Methanol is a well-known hole scavenger from photoexcited metal oxides(36-38) indicating that adsorbed methanol contains an occupied state that could be acting as a hole

acceptor from the Co_3O_4 valence band. Accordingly, of the possibilities considered here, it seems most probable that hole transfer from photoexcited Co_3O_4 to the methanol surface layer is the first step leading to surface-mediated recombination. In this mechanism, we can neglect the possibility of hole thermalization from an O 2p orbital to a Co 3d orbital in the valence band of Co_3O_4 prior to injection because this process would be observed as a change in the transient absorption spectrum corresponding to either the $Co^{2+} \rightarrow Co^{3+}$ MMCT state or the Co^{3+} d–d excited state shown in Supporting Information Figure S7. Because neither of these states is observed as intermediates in the transient absorption kinetics, we hypothesize that hole injection to methanol occurs directly from the O 2p orbital of Co_3O_4.

In this picture, hole injection to the methanol represents the driving force for surface trapping of the free electrons as positive charges accumulate in the adsorbed methanol layer. Another way of stating this is that in the absence of an interface potential to drive charge separation, the exciton remains bound, and when the hole is trapped in the adsorbed methanol layer, the electron also remains localized to the near surface region. Because the rate of surface trapping appears to be near the diffusion limit for carrier migration, this mechanism would suggest that hole transfer from the O 2p orbital of Co_3O_4 to surface methanol is reasonably efficient. If this mechanism is correct, then these results point to recombination of electrons with partially oxidized surface intermediates as a possible reason that direct excitation of Co_3O_4 does not lead to high photocatalytic redox efficiency. It is also possible that surface charge trapping leads to increased exciton concentration in the near-surface region resulting in enhanced Auger recombination, even at these longer time scales. This study explores the important role of surface electronic structure to influence excited state evolution and relaxation lifetimes in nanoscale systems and demonstrates the ability of HHG transient absorption spectroscopy to follow these dynamics in liquid environments in real time with chemical state specificity. For these reasons we anticipate that this technique will find additional applications studying a wide range of catalytic and energy conversion processes occurring at the solid–liquid interface.

Methods

High Harmonic Generation Transient Absorption Spectrometer

The details of the HHG transient absorption spectrometer have been reported elsewhere.(35) In short, high harmonics are generated by focusing an 800 nm pump pulse (1.5 mJ, 35 fs) into a semi-infinite gas cell containing 100 Torr of Ne. A 400 nm pulse (20 μJ, 60 fs) is used as a symmetry breaking field to allow generation of both even and odd harmonics. The residual 800 and 400 nm light is removed from the high harmonic EUV beam using two 600 nm thick Al filters. A gold-coated toroidal mirror at grazing incidence focuses the EUV beam onto the Co_3O_4 sample. After the sample, the transmitted beam is spectrally dispersed

onto a CCD detector using a concave variable line spacing grating. The entire system after the semi-infinite gas cell is maintained at 10^{-6} Torr. The sample is pumped with a separate 400 nm pulse (3.0 μJ, 35 fs) focused to a spot size of 150 μm.

To obtain a transient spectrum, a shutter is used to block the pump beam and the difference spectrum is recorded. Spectra are integrated for 2–3 s depending on the X-ray transmission, which varies between the vacuum and methanol samples. The data reported here reflect the average of 200 spectra per time point. All reported data in methanol were collected using a single Co_3O_4 substrate. Data were collected from multiple sample locations. Between 4 and 6 runs a day for 5 days were collected on this sample to produce the data set. Difference spectra recorded at negative time delays are nonzero. This represents the combined effect of transient states that have lifetimes >1 ms (the repetition rate of the laser) as well as solvent bleaching by the pump beam that was found to recover on the several second time scale. Consequently, in the reported data the transient absorption recorded at negative delay times is subtracted to remove these contributions to the spectra.

To avoid sample damage caused by laser-induced heating, the vacuum samples are raster scanned as described previously.(35) However, unlike the vacuum samples, the methanol samples were not raster scanned because the presence of methanol greatly reduces laser heating, and no beam-induced spectral changes were observed, even after several hours of pump beam exposure.

Liquid Cell

A silicon nitride liquid cell was used to adapt the transient absorption spectrometer to liquid phase samples for studies of the solid/liquid interface. Similar cells have been previously used for static or time-resolved soft X-ray absorption measurements in the liquid phase.(63, 64) The cell consists of two silicon nitride membranes (100 nm each) supported on silicon substrates and separated by an SU8 polymer spacer layer (500 nm). The cobalt oxide catalyst is deposited on one of these membranes. During experiments, these two substrates are pressed face-to-face and inlet and outlet lines are connected to the liquid channel via O-ring seals. A schematic of this liquid cell is depicted in Supporting Information Figure S8.

Because the thin silicon nitride membranes will bend outward or burst if the methanol is pressurized inside the liquid cell, a syringe pump is used to pull vacuum on the outlet side of the cell while the inlet side is supplied with methanol at ambient pressure. This method for flowing relies on capillary action and ensures that pressure inside the cell never exceeds 1 bar. In accordance with capillary-driven flow, we find that the flow rate depends on the contact angle of the solvent on the surface of the liquid cell. In the case of aqueous solvent, UV/ozone treatment of the substrate is necessary to make the surface hydrophilic in order to create a capillary pressure. However, methanol wets the substrate even without any pretreatment, and no surface pretreatment was used in these experiments. On the basis of the migration of air bubbles in the liquid cell feed

lines, it is estimated that the flow rate is on the order of 100 nL/min.

Co_3O_4 Thin Film Preparation

Co_3O_4 thin films were prepared by magnetron sputtering from a metallic Co source in an Ar atmosphere. As-deposited the films were both amorphous and highly O deficient. However, annealing the films at 500 °C for 12 h in air resulted in a pure crystalline spinel Co_3O_4 phase as confirmed by both X-ray diffraction and electron diffraction (see Supporting Information Figure S9). On the basis of the measured sputter rate, the Co_3O_4 films were 15 nm thick after annealing.

Supporting Information

Spectral response of methanol to 400 nm pump beam, solutions and plots of kinetic models, results of ligand field multiplet simulation, schematic of liquid flow cell, electron diffractogram, transmission electron micrograph, and UV/vis/NIR extinction spectrum of Co_3O_4 thin films. This material is available free of charge via the Internet at http://pubs.acs.org.

Author Present Address
(L.R.B.) Department of Chemistry and Biochemistry, The Ohio State University, Columbus, OH 43210.
Author Present Address
(J.V.-W.) Department of Chemistry, University of Illinois at Urbana–Champaign, Urbana, IL 61801.

The authors declare no competing financial interest.

•

Acknowledgment

This work is supported by the Materials Science Division of Lawrence Berkeley National Laboratory by the U.S. Department of Energy at Lawrence Berkeley National Lab under Contract No. DE-AC02-05CH11231, “Physical Chemistry of Nanomaterials.” Initial work by C.-M.J. and instrument construction were supported by the NSF Engineering Research Center for Extreme Ultraviolet Science and Technology (EEC-0310717). L.R.B. is supported by the Office of Assistant Secretary of Defense for Research and Engineering, National Security Science and Engineering Faculty Fellowship granted to S.R.L. S.T.K. and M.K.G. acknowledge support from a Lawrence Berkeley National Lab Laboratory Directed Research and Development grant for development of the liquid flow cell and from the Condensed Phase and Interfacial Molecular Sciences Program of the U.S. Department of Energy also under Contract DE-AC02-05CH11231. J.M.L. is supported as part of the Light-Material Interactions in Energy Conversion, an Energy Frontier Research Center funded by the U.S. Department of Energy, Office of Science, Office of Basic Energy Sciences, under Contract DE-SC0001293. Brandon J. Beberwyck and Daniel J. Hellebusch are thanked for help with measurement and analysis of electron diffraction data.

•

References

This article references 64 other publications.

1. Adams, D. M.; Brus, L.; Chidsey, C. E. D.; Creager, S.; Creutz, C.; Kagan, C. R.; Kamat, P. V.; Lieberman, M.; Lindsay, S.; Marcus, R. A.; Metzger, R. M.; Michel-Beyerle, M. E.; Miller, J. R.; Newton, M. D.; Rolison, D. R.; Sankey, O.; Schanze, K. S.; Yardley, J.; Zhu, X. *J. Phys. Chem. B* **2003**, 107, 6668[ACS Full Text], [CAS]
2. Bazant, M. Z. *Acc. Chem. Res.* **2013**, 46, 1144[ACS Full Text], [PubMed], [CAS]
3. Zhang, C.; Grass, M. E.; McDaniel, A. H.; DeCaluwe, S. C.; Gabaly, F. E.; Liu, Z.; McCarty, K. F.; Farrow, R. L.; Linne, M. A.; Hussain, Z.; Jackson, G. S.; Bluhm, H.; Eichhorn, B. W. *Nat. Mater.* **2010**, 9, 944[CrossRef], [PubMed], [CAS]
4. Britto, P. J.; Santhanam, K. S. V.; Rubio, A.; Alonso, J. A.; Ajayan, P. M. *Adv. Mater.* **1999**, 11, 154[CrossRef], [CAS]
5. Abe, T.; Fukuda, H.; Iriyama, Y.; Ogumi, Z. *J. Electrochem. Soc.* **2004**, 151, A1120[CrossRef], [CAS]
6. Li, J.; Xiao, X.; Cheng, Y.-T.; Verbrugge, M. W. *J. Phys. Chem. Lett.* **2013**, 3387[ACS Full Text], [PubMed], [CAS]
7. Subbaraman, R.; Tripkovic, D.; Chang, K.-C.; Strmcnik, D.; Paulikas, A. P.; Hirunsit, P.; Chan, M.; Greeley, J.; Stamenkovic, V.; Markovic, N. M. *Nat. Mater.* **2012**, 11, 550[CrossRef], [PubMed], [CAS]
8. Wang, Y.; Velmurugan, J.; Mirkin, M. V. *Isr. J. Chem.* **2010**, 50, 291[CrossRef], [CAS]
9. Fujishima, A.; Honda, K. *Nature* **1972**, 238, 37[CrossRef], [PubMed], [CAS]
10. O'Regan, B.; Gratzel, M. *Nature* **1991**, 353, 737[CrossRef], [CAS]
11. An, J.; Kim, Y.-B.; Gür, T. M.; Prinz, F. B. *ACS Appl. Mater. Interfaces* **2012**, 4, 6790[ACS Full Text], [PubMed], [CAS]
12. Liaw, B. Y. *Electrode-Electrolyte Interfaces in Li-ion Batteries*; Electrochemical Society: Pennington, NJ, USA, **2011**.
13. Peled, E. *J. Electrochem. Soc.* **1979**, 126, 2047[CrossRef], [CAS]
14. Fabregat-Santiago, F.; Garcia-Belmonte, G.; Bisquert, J.; Zaban, A.; Salvador, P. *J. Phys. Chem. B* **2001**, 106, 334[ACS Full Text]
15. Henderson, M. A.; White, J. M.; Uetsuka, H.; Onishi, H. *J. Am. Chem. Soc.* **2003**, 125, 14974[ACS Full Text], [PubMed], [CAS]
16. Graetzel, M.; Janssen, R. A. J.; Mitzi, D. B.; Sargent, E. H. *Nature* **2012**, 488, 304[CrossRef], [PubMed], [CAS]
17. Reeja-Jayan, B.; Adachi, T.; Ono, R. J.; Vanden Bout, D. A.; Bielawski, C. W.; Manthiram, A. *J. Mater. Chem. A* **2013**, 1, 3258[CrossRef], [CAS]
18. Park, D.-W.; Jeong, Y.; Lee, J.; Lee, J.; Moon, S.-H. *J. Phys. Chem. C* **2013**, 117, 2734[ACS Full Text], [CAS]
19. Galland, C.; Ghosh, Y.; Steinbruck, A.; Sykora, M.; Hollingsworth, J. A.; Klimov, V. I.; Htoon, H. *Nature* **2011**, 479, 203[CrossRef], [PubMed],

[CAS]
20. Cordones, A. A.; Scheele, M.; Alivisatos, A. P.; Leone, S. R. *J. Am. Chem. Soc.* **2012**, 134, 18366[ACS Full Text], [PubMed], [CAS]
21. Knowles, K. E.; Tice, D. B.; McArthur, E. A.; Solomon, G. C.; Weiss, E. A. *J. Am. Chem. Soc.* **2009**, 132, 1041[ACS Full Text]
22. Morris-Cohen, A. J.; Frederick, M. T.; Cass, L. C.; Weiss, E. A. *J. Am. Chem. Soc.* **2011**, 133, 10146[ACS Full Text], [PubMed], [CAS]
23. Somorjai, G. A.; Beaumont, S. K.; Alayoglu, S. *Angew. Chem., Int. Ed.* **2011**, 50, 10116[CrossRef], [CAS]
24. Tao, F.; Dag, S.; Wang, L.-W.; Liu, Z.; Butcher, D. R.; Bluhm, H.; Salmeron, M.; Somorjai, G. A. *Science* **2010**, 327, 850[CrossRef], [PubMed], [CAS]
25. Tao, F.; Grass, M. E.; Zhang, Y.; Butcher, D. R.; Renzas, J. R.; Liu, Z.; Chung, J. Y.; Mun, B. S.; Salmeron, M.; Somorjai, G. A. *Science* **2008**, 322, 932[CrossRef], [PubMed], [CAS]
26. Gilbert, B.; Katz, J. E.; Huse, N.; Zhang, X.; Frandsen, C.; Falcone, R. W.; Waychunas, G. A. *Phys. Chem. Chem. Phys.* **2013**, 15, 17303[CrossRef], [PubMed], [CAS]
27. Canton, S. E.; Zhang, X.; Zhang, J.; van Driel, T. B.; Kjaer, K. S.; Haldrup, K.; Chabera, P.; Harlang, T.; Suarez-Alcantara, K.; Liu, Y.; Pérez, J.; Bordage, A.; Pápai, M.; Vankó, G.; Jennings, G.; Kurtz, C. A.; Rovezzi, M.; Glatzel, P.; Smolentsev, G.; Uhlig, J.; Dohn, A. O.; Christensen, M.; Galler, A.; Gawelda, W.; Bressler, C.; Lemke, H. T.; Møller, K. B.; Nielsen, M. M.; Lomoth, R.; Wärnmark, K.; Sundström, V. *J. Phys. Chem. Lett.* **2013**, 4, 1972[ACS Full Text], [CAS]
28. Tamaki, Y.; Furube, A.; Murai, M.; Hara, K.; Katoh, R.; Tachiya, M. *J. Am. Chem. Soc.* **2005**, 128, 416[ACS Full Text]
29. Yang, X.; Tamai, N. *Phys. Chem. Chem. Phys.* **2001**, 3, 3393[CrossRef], [CAS]
30. Ghosh, H. N.; Asbury, J. B.; Lian, T. *J. Phys. Chem. B* **1998**, 102, 6482[ACS Full Text], [CAS]
31. Asbury, J. B.; Ellingson, R. J.; Ghosh, H. N.; Ferrere, S.; Nozik, A. J.; Lian, T. *J. Phys. Chem. B* **1999**, 103, 3110[ACS Full Text], [CAS]
32. Yoshihara, T.; Katoh, R.; Furube, A.; Tamaki, Y.; Murai, M.; Hara, K.; Murata, S.; Arakawa, H.; Tachiya, M. *J. Phys. Chem. B* **2004**, 108, 3817[ACS Full Text], [CAS]
33. Chen, H.-Y.; Chen, T.-Y.; Son, D. H. *J. Phys. Chem. C* **2010**, 114, 4418[ACS Full Text], [CAS]
34. Wu, K.; Rodríguez-Córdoba, W.; Lian, T. *J. Phys. Chem. B* **2014**, , DOI: 10.1021/jp504703t [ACS Full Text]
35. Vura-Weis, J.; Jiang, C.-M.; Liu, C.; Gao, H.; Lucas, J. M.; de Groot, F. M. F.; Yang, P.; Alivisatos, A. P.; Leone, S. R. *J. Phys. Chem. Lett.* **2013**, 3667[ACS Full Text], [PubMed], [CAS]
36. Yamakata, A.; Ishibashi, T.-a.; Onishi, H. *J. Phys. Chem. B* **2002**, 106,

9122[ACS Full Text], [CAS]
37. Shen, M.; Henderson, M. A. *J. Phys. Chem. Lett.* **2011**, 2, 2707[ACS Full Text], [CAS]
38. Howe, R. F.; Gratzel, M. *J. Phys. Chem.* **1985**, 89, 4495[ACS Full Text], [CAS]
39. Crepaldi, A.; Moreschini, L.; Autès, G.; Tournier-Colletta, C.; Moser, S.; Virk, N.; Berger, H.; Bugnon, P.; Chang, Y. J.; Kern, K.; Bostwick, A.; Rotenberg, E.; Yazyev, O. V.; Grioni, M. *Phys. Rev. Lett.* **2012**, 109, 096803[CrossRef], [CAS]
40. Jung, T.; Dodabalapur, A.; Wenz, R.; Mohapatra, S. *Appl. Phys. Lett.* **2005**, 87
41. Reineke, R.; Memming, R. *J. Phys. Chem.* **1992**, 96, 1317[ACS Full Text], [CAS]
42. Shi, F.; Baker, L. R.; Hervier, A.; Somorjai, G. A.; Komvopoulos, K. *Nano Lett.* **2013**, 13, 4469[ACS Full Text], [PubMed], [CAS]
43. Kanan, M. W.; Nocera, D. G. *Science* **2008**, 321, 1072[CrossRef], [PubMed], [CAS]
44. Jiao, F.; Frei, H. *Angew. Chem., Int. Ed.* **2009**, 48, 1841[CrossRef], [PubMed], [CAS]
45. Jiao, F.; Frei, H. *Energy Environ. Sci.* **2010**, 3, 1018[CrossRef], [CAS]
46. Yusuf, S.; Jiao, F. *ACS Catal.* **2012**, 2, 2753[ACS Full Text], [CAS]
47. Rosen, J.; Hutchings, G. S.; Jiao, F. *J. Am. Chem. Soc.* **2013**, 135, 4516[ACS Full Text], [PubMed], [CAS]
48. Hara, M.; Waraksa, C. C.; Lean, J. T.; Lewis, B. A.; Mallouk, T. E. *J. Phys. Chem. A* **2000**, 104, 5275[ACS Full Text], [CAS]
49. Harriman, A.; Richoux, M.-C.; Christensen, P. A.; Mosseri, S.; Neta, P. *J. Chem. Soc., Faraday Trans. 1* **1987**, 83, 3001[CrossRef], [CAS]
50. Harriman, A.; Pickering, I. J.; Thomas, J. M.; Christensen, P. A. *J. Chem. Soc., Faraday Trans. 1* **1988**, 84, 2795[CrossRef], [CAS]
51. Jiang, C. M.; Baker, L. R.; Lucas, J. M.; Vura-Weis, J.; Alivisatos, A. P.; Leone, S. R. *J. Phys. Chem. C* **2014**, , DOI: 10.1021/jp5071133 [ACS Full Text]
52. Snellenburg, J. J.; Laptenok, S.; Seger, R.; Mullen, K. M.; Stokkum, I. H. M. v. *J. Stat. Software* **2012**, 49, 1[CrossRef]
53. Stavitski, E.; de Groot, F. M. F. *Micron* **2010**, 41, 687[CrossRef], [PubMed], [CAS]
54. de Groot, F. *Chem. Rev.* **2001**, 101, 1779[ACS Full Text], [PubMed], [CAS]
55. de Groot, F.; Kotani, A. *Core Level Spectroscopy of Solids*; Taylor & Francis: Oxford, U.K., **2008**.[CrossRef]
56. Morales, F.; de Groot, F. M. F.; Glatzel, P.; Kleimenov, E.; Bluhm, H.; Hävecker, M.; Knop-Gericke, A.; Weckhuysen, B. M. *J. Phys. Chem. B* **2004**, 108, 16201[ACS Full Text], [CAS]
57. Kim, K. J.; Park, Y. R. *Solid State Commun.* **2003**, 127, 25[CrossRef],

[CAS]
58. Almand-Hunter, A. E.; Li, H.; Cundiff, S. T.; Mootz, M.; Kira, M.; Koch, S. W. *Nature* **2014**, 506, 471[CrossRef], [PubMed], [CAS]
59. Tang, H.; Prasad, K.; Sanjinès, R.; Schmid, P. E.; Lévy, F. *J. Appl. Phys.* **1994**, 75, 2042[CrossRef], [CAS]
60. Jose, R.; Thavasi, V.; Ramakrishna, S. *J. Am. Ceram. Soc.* **2009**, 92, 289[CrossRef], [CAS]
61. Zhao, J.; Li, B.; Onda, K.; Feng, M.; Petek, H. *Chem. Rev.* **2006**, 106, 4402[ACS Full Text], [PubMed], [CAS]
62. Szymanski, P.; Garrett-Roe, S.; Harris, C. B. *Prog. Surf. Sci.* **2005**, 78, 1[CrossRef], [CAS]
63. Schreck, S.; Gavrila, G.; Weniger, C.; Wernet, P. *Rev. Sci. Instrum.* **2011**, 82
64. Huse, N.; Cho, H.; Hong, K.; Jamula, L.; de Groot, F. M. F.; Kim, T. K.; McCusker, J. K.; Schoenlein, R. W. *J. Phys. Chem. Lett.* **2011**, 2, 880[ACS Full Text], [PubMed], [CAS]